arXiv:1606.04785v2 [cond-mat.str-el] 23 Aug 2016

Computation of dynamical correlation functions for many fermion systems with auxiliary-field quantum Monte Carlo

Ettore Vitali,[1] Hao Shi,[1] Mingpu Qin,[1] and Shiwei Zhang[1]

[1] *Department of Physics, The College of William and Mary, Williamsburg, Virginia 23187*

We address the calculation of dynamical correlation functions for many fermion systems at zero temperature, using the auxiliary-field quantum Monte Carlo method. The two-dimensional Hubbard hamiltonian is used as a model system. Although most of the calculations performed here are for cases where the sign problem is absent, the discussions are kept general for applications to physical problems when the sign problem does arise. We study the use of twisted boundary conditions to improve the extrapolation of the results to the thermodynamic limit. A strategy is proposed to drastically reduce finite size effects relying on a minimization among the twist angles. This approach is demonstrated by computing the charge gap at half-filling. We obtain accurate results showing the scaling of the gap with the interaction strength U, connecting to the scaling of the unrestricted Hartree-Fock method at small U and Bethe Ansatz exact result in one dimension at large U. A new algorithm is then proposed to compute dynamical Green functions and correlation functions which explicitly varies the number of particles during the random walks in the manifold of Slater determinants. In dilute systems, such as ultracold Fermi gases, this algorithm enables calculations with much more favorable complexity, with computational cost proportional to basis size or the number of lattice sites.

PACS numbers: 02.70.Ss, 71.27.+a, 71.10.Fd, 03.75.Ss

I. INTRODUCTION

The calculation of dynamical correlation functions of many-body quantum systems is a great challenge in theoretical condensed matter physics. Such functions provide a unique opportunity to explore the manifold of the excited states of a physical system. They often provide a much more direct connection to experimental measurements, giving access to crucial properties such as spectral functions, excitation spectra, and charge and spin gaps, to name a few.

With the advent of modern computational resources, quantum Monte Carlo (QMC) simulations[1–4] are becoming a very powerful tool for computations in quantum many-particle models and realistic systems. A vast array of total energy and related quantities have been computed. Equal-time correlation functions have also been studied fairly routinely by QMC, especially in model systems. To estimate dynamical properties from first principles using QMC has been more challenging. Important results have been obtained for bosonic strongly correlated systems.[5–11] Also excited states of low dimensional bosonic systems have been recently studied[12,13]. For fermionic systems, in special situations where the sign problem is not present, accurate calculations have been performed[14–17]. A few attempts have been also made[14,18–21] in the more difficult situations where approximations are needed to deal with the sign problem[22–26].

In this paper we study the calculation of imaginary-time correlation functions and excited state information in interacting fermion systems at zero temperature. We formulate and discuss our methods in a general framework, keeping in mind applications in many-fermion systems where a sign problem arises and a constrained path approach is applied within an open-ended imaginary-time projection. Most of our illustrations and applications in the present paper, however, will be in systems where the sign problem is absent and exact results can be obtained. For these we use the two-dimensional Hubbard hamiltonian with repulsive interaction at half-filling. We employ the path-integral auxiliary-field quantum Monte Carlo (AFQMC) framework, but including a force-bias acceleration technique[27] in the Metropolis sampling and a technique to control Monte Carlo variance divergence[28].

In the first part of the paper, we implement a standard approach[15,29] of computing non-equal-time Green functions and correlation functions within AFQMC. Our focus is on the extrapolation of the results to the thermodynamic limit and testing the efficiency of different implementations in general many-fermion systems. We show that it is convenient to introduce twisted boundary conditions[30], and suggest a way to exploit the boundary conditions that dramatically reduces finite-size effects in the calculation of the charge gap. Accurate results for the gap are obtained in the repulsive Hubbard model even at weak interactions, which mimic many real materials where the gap might be very small compared to the energy scales, presenting challenges for numerical calculations. With our approach, the charge gap is determined even at U/t as small as 0.5, far beyond the reach of previous unbiased many-body calculations.

In the second part, we propose a new algorithm to compute dynamical Green functions, density-density and spin-spin correlation functions which, in the dilute limit, dramatically reduces the complexity without affecting the numerical stability of the calculations or the accuracy of the results. The method relies on the explicit variation of the number of particles during the random walk in the manifold of Slater determinants. We show that,

for example, the spectral function for one given momentum can be calculated with a computational complexity proportional to the number of lattice sites, which enables simulations on very large lattices. The new method will have great advantages in systems such as atomic Fermi gases, which can be modeled by the attractive Hubbard model in the dilute limit[31], or real materials, where the calculations typically require[26] a basis size much larger than the number of electrons.

The reminder of this paper is organized as follows. In Sec. II we will briefly sketch the AFQMC methodology, and then describe our implementation of a stable algorithm to compute dynamical Green functions, both in the path-integral (for sign-problem-free systems) and open-ended random walk (for constrained path calculations when the sign problem is present). In Sec. III, we propose a strategy to control finite-size effects using twisted boundary conditions, and present our results for the charge gap in the repulsive Hubbard model at half-filling in the intermediate and weakly interacting regime. In Sec. IV we describe our new approach which, in the dilute limit, dramatically improves the complexity of the calculations. We conclude in Sec. V.

II. AUXILIARY FIELD QUANTUM MONTE CARLO FORMALISM

We introduce the basic notations of the methodology using the Hubbard hamiltonian which, as mentioned, will be our model system:

$$\hat{H} = -t \sum_{<i,j>,\sigma=\uparrow,\downarrow} \hat{c}^{\dagger}_{i,\sigma}\hat{c}_{j,\sigma} + U \sum_{i} \left(\hat{n}_{i,\uparrow} - \frac{1}{2}\right)\left(\hat{n}_{i,\downarrow} - \frac{1}{2}\right) \tag{1}$$

where the labels i, j run over the sites of a square lattice with $\mathcal{N}_s = L_x \times L_y = L^2$ sites, the symbol $<,>$ denotes, as usual, nearest neighbors and $\hat{n}_{i,\sigma} = \hat{c}^{\dagger}_{i,\sigma}\hat{c}_{i,\sigma}$ is the particle number density operator on site i for the given spin direction σ. The Hubbard model[32,33] is one of the most widely studied models in condensed matter physics. It is of fundamental theoretical importance in the context of magnetism and cuprate superconductors, and is relevant to experiments using ultracold fermionic atoms both in a trap (in the continuum) and in optical lattices. Despite its simplicity, no analytical solutions to this Hamiltonian are known beyond the perturbative limit. The model provides an excellent test ground for many-body theories and computational approaches.

Denoting by $|\phi_T\rangle$ a Slater determinant with $N_\uparrow$ spin-up and $N_\downarrow$ spin-down particles, provided that $|\phi_T\rangle$ is not orthogonal to the $\mathcal{N}_p$-particle ($\mathcal{N}_p = N_\uparrow + N_\downarrow$) ground state $|\,\Psi_0\,\rangle$ of (1), the following relation holds:

$$|\,\Psi_0\rangle \propto \lim_{\beta\to+\infty} e^{-\beta(\hat{H}-E_0)}|\phi_T\rangle \tag{2}$$

where E_0 is an estimate of the ground state energy. A combined use of Trotter-Suzuki breakup and Hubbard-Stratonovich transformation provides the following approximation:

$$e^{-\beta(\hat{H}-E_0)} = \left(e^{-\delta\tau(\hat{H}-E_0)}\right)^M \simeq \left(\int d\mathbf{x} p(\mathbf{x})\hat{B}(\mathbf{x})\right)^M \tag{3}$$

where $\mathbf{x} = (x_1, \ldots, x_{\mathcal{N}_s})$ is an auxiliary field (often discrete Ising fields on the lattice), $\hat{B}(\mathbf{x})$ is a one-particle propagator, and $\delta\tau = \beta/M$ is a sufficiently small *time-step*. The function $p(\mathbf{x})$ is a probability density.

In the repulsive Hubbard model, for example, the simplest way to build the approximation in Eq. (3) is to use the following discrete spin decomposition of the Hubbard-Stratonovich transformation:

$$e^{-\delta\tau U \hat{n}_{i,\uparrow}\hat{n}_{i,\downarrow}} = \sum_{x_i=\pm 1} \frac{1}{2}\hat{b}_i(x_i) \tag{4}$$

where:

$$\hat{b}_i(x) = e^{-\delta\tau U \frac{\hat{n}_{i,\uparrow}+\hat{n}_{i,\downarrow}}{2}}\, e^{-\gamma x(\hat{n}_{i,\uparrow}-\hat{n}_{i,\downarrow})} \tag{5}$$

where $\cosh(\gamma) = \exp(\delta\tau U/2)$. Different forms of the decomposition can affect the accuracy and efficiency of the calculation[34,35], but will not affect the formalism discussed in the rest of the paper.

A key point of the methodology is that the operator $\hat{B}(\mathbf{x})$ appearing in Eq. (3) is the exponential of a one-body operator dependent on the auxiliary field configuration. We can write:

$$\hat{B}(\mathbf{x}) = \exp\left(\sum_{\mathbf{i}\sigma,\mathbf{j}\sigma'} \mathcal{A}_{\mathbf{i}\sigma,\mathbf{j}\sigma'}(\mathbf{x})\;\; \hat{\mathbf{c}}^{\dagger}_{\mathbf{i},\sigma}\,\hat{\mathbf{c}}_{\mathbf{j},\sigma'}\right) \tag{6}$$

where the explicit form of the $\mathcal{N}_s \times \mathcal{N}_s$-matrix $\mathcal{A}(\mathbf{x})$ depends on the choice of the Hubbard-Stratonovich transformation. For the description of the formalism, it will turn out to be useful to introduce the matrix:

$$\mathcal{B}(\mathbf{x}) = \exp\left(\mathcal{A}(\mathbf{x})\right)\,. \tag{7}$$

Any operator $\hat{B}(\mathbf{x})$ operating on a Slater determinant $|\phi\rangle$ results in another Slater determinant $|\phi'\rangle$, given in matrix form by

$$\mathcal{B}(\mathbf{x})\mathbf{\Phi} = \mathbf{\Phi}'\,, \tag{8}$$

where $\Phi = \Phi_\uparrow \otimes \Phi_\downarrow$, with Φ_σ being the $\mathcal{N}_s \times N_\sigma$ matrix containing the spin-σ orbitals of the Slater determinant wave function $|\phi\rangle$, and similarly for $|\phi'\rangle$.

A. Static properties

The standard path-integral AFQMC method allows the evaluation of ground state expectation values:

$$\langle\hat{O}\rangle = \frac{\langle\Psi_0|\,\hat{O}\,|\Psi_0\rangle}{\langle\Psi_0\,|\,\Psi_0\rangle} \tag{9}$$

by casting them in the following form:

$$\langle \hat{O} \rangle = \int d\mathbf{X}\, \mathcal{W}(\mathbf{X})\, \mathcal{O}(\mathbf{X})\,. \tag{10}$$

In Eq. (10), $\mathbf{X} = (\mathbf{x}(1), \ldots, \mathbf{x}(M))$ denotes a (discretized) *path* in auxiliary fields configurational space. Moreover, if we introduce the two Slater Determinants:

$$\langle \phi_L| \;= \langle \phi_T|\, \hat{B}(\mathbf{x}(M)) \ldots \hat{B}(\mathbf{x}(l)) \tag{11}$$

and:

$$|\phi_R\rangle = \hat{B}(\mathbf{x}(l-1)) \ldots \hat{B}(\mathbf{x}(1))\, |\phi_T\rangle\,, \tag{12}$$

we may write:

$$\mathcal{W}(\mathbf{X}) \propto \langle \phi_L \,|\, \phi_R \rangle \prod_{i=1}^{M} p(\mathbf{x}(i)) \tag{13}$$

and:

$$\mathcal{O}(\mathbf{X}) = \frac{\langle \phi_L|\, \hat{O}\, |\phi_R\rangle}{\langle \phi_L \,|\, \phi_R\rangle} \tag{14}$$

Whenever $\mathcal{W}(\mathbf{X}) \geq 0$ for each auxiliary field configurations, as it happens if $U < 0$ and $N_\uparrow = N_\downarrow$ or at half-filling ($\mathcal{N}_p = \mathcal{N}_s$) when $U > 0$, the integral in (10) can be evaluated via Monte Carlo. We use an efficient Metropolis sampling of the paths, exploiting a force bias[2,27] that allows high acceptance ratio in the updates of the path in the auxiliary field configuration space, and eliminating the infinite variance problem[28] with a bridge link approach.

When a sign problem is present, a constrained path[25] or phase-free approximation[26] can be imposed to remove the exponentially growing noise (with system size or the length of the path β) and restore the same computational scaling as in the sign-problem-free cases. The paths become open-ended. The primary difference is that $\langle \phi_L|$ is now produced by back-propagation (BP)[2], and a weight accompanies each path. The details of the back-propagation for static properties have been discussed elsewhere[36]. The modification to compute dynamical properties is minimal beyond what is necessary for the path-integral formalism, and we will comment on it as needed below.

B. Dynamical properties

Dynamical correlation functions in imaginary-time at zero temperature have the general form:

$$f(\tau) = \frac{\langle \Psi_0|\, \hat{A}\, e^{-\tau(\hat{H}-E_0)}\, \hat{B}\, |\Psi_0\rangle}{\langle \Psi_0 \,|\, \Psi_0\rangle} \tag{15}$$

where $\hat{A}$ and $\hat{B}$ can be destruction or creation operators, or one-body operators such as the particle density or the spin density or even more general operators.

Let us focus on the dynamical *particles* and *holes* Green functions in imaginary-time, i.e. the matrices:

$${G^p}_{i\sigma,j\sigma'}(\tau) = \frac{\langle \Psi_0|\, \hat{c}_{i,\sigma}\, e^{-\tau(\hat{H}-E_0)}\, \hat{c}^\dagger_{j,\sigma'}\, |\Psi_0\rangle}{\langle \Psi_0 \,|\, \Psi_0\rangle} \tag{16}$$

and:

$${G^h}_{i\sigma,j\sigma'}(\tau) = \frac{\langle \Psi_0|\, \hat{c}^\dagger_{i,\sigma}\, e^{-\tau(\hat{H}-E_0)}\, \hat{c}_{j,\sigma'}\, |\Psi_0\rangle}{\langle \Psi_0 \,|\, \Psi_0\rangle}\,. \tag{17}$$

When the Hamiltonian is spin-independent as is the case in the Hubbard model, all the terms with $\sigma \neq \sigma'$ identically vanish. In order to keep the notations simple, we will work for $\sigma = \uparrow$ (the other case being analogous) and neglect the spin index. Dealing with translationally invariant systems, we will denote ${G^{p,h}}_{i\sigma,j\sigma}(\tau)$ by $G^{p,h}(R,\tau)$ with $R = (i-j)$. The Fourier transforms, i.e., the dynamical Green functions in momentum space, will be denoted by $\tilde{G}^{p,h}(Q,\tau)$, where $Q = (Q_x, Q_y)$ is a wave-vector of the reciprocal lattice: $Q_x = \frac{2\pi}{L_x}\, n_x$, with $n_x \in \{0, \ldots, L_x - 1\}$, and similarly for Q_y.

The imaginary-time propagator between the operators $\hat{A}$ and $\hat{B}$ can again be expressed using Eq. (3). This can be thought of as inserting an extra segment to the path we keep: a number $N_\tau = \tau/\delta\tau$ of *time-slices*, say $\tilde{\mathbf{x}}(1), \ldots, \tilde{\mathbf{x}}(N_\tau)$. The static estimator Eq. (14) is replaced by a dynamical estimator which (for example in the case of the particles Green function) can be cast in the form (see Ref. 14):

$$g(\mathbf{X},\tau) = \frac{\langle \phi_L|\, \hat{c}_i\, \hat{B}(\tilde{\mathbf{x}}(N_\tau)) \ldots \hat{B}(\tilde{\mathbf{x}}(1))\; \hat{c}^\dagger_j |\phi_R\rangle}{\langle \phi_L\, |\hat{B}(\tilde{\mathbf{x}}(N_\tau)) \ldots \hat{B}(\tilde{\mathbf{x}}(1))\, |\, \phi_R\rangle} \tag{18}$$

To keep the notation simple, we will write $\hat{B}_i$ instead of $\hat{B}(\tilde{\mathbf{x}}(i))$ from now on.

In order to calculate Eq. (18) for a given configuration of auxiliary fields, we use the manipulations presented in Ref. 15. We introduce the equal-time Green function matrix:

$$\mathcal{G}^p(n,n) = \frac{\langle \phi_L \,|\, \hat{B}_{N_\tau} \ldots \hat{B}_{n+1}\, \hat{c}_i\, \hat{c}^\dagger_j\, \hat{B}_n \hat{B}_{n-1} \ldots\;\; \hat{B}_1 |\phi_R\rangle}{\langle \phi_L \,|\; \hat{B}_{N_\tau} \ldots \hat{B}_1\; |\phi_R\rangle} \tag{19}$$

and the time displaced one:

$$\mathcal{G}^p(n,m) = \frac{\langle \phi_L \,|\, \hat{B}_{N_\tau} .. \hat{B}_{n+1}\, \hat{c}_i\;\, \hat{B}_n .. \hat{B}_{m+1}\;\, \hat{c}^\dagger_j\, \hat{B}_m .. \hat{B}_1 |\phi_R\rangle}{\langle \phi_L \,|\; \hat{B}_{N_\tau} \ldots \hat{B}_1\; |\phi_R\rangle}\,. \tag{20}$$

The central result is provided by the following:

$$\mathcal{G}^p(n,m) = \mathcal{G}^p(n,n-1)\mathcal{G}^p(n-1,n-2) \ldots \mathcal{G}^p(m+1,m) \tag{21}$$

and:

$$\mathcal{G}^p(l,l-1) = \mathcal{G}^p(l,l)\mathcal{B}_l \tag{22}$$

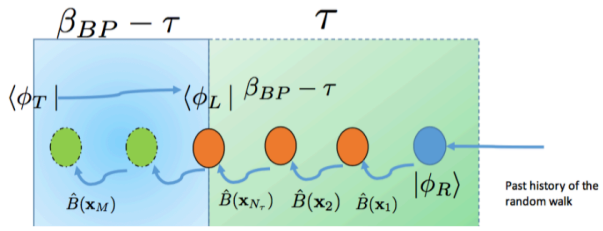

FIG. 1. (color online) The calculation of imaginary-time correlation functions in an open-ended branching random walk: a sketch of the implementation.

where $\mathcal{B}_l \equiv \mathcal{B}(\tilde{\mathbf{x}}(\mathbf{l}))$ is the matrix of Eq. (7). These identies are straightforward to show using the commutators between the propagator and the creation or annihilation operators[37,38]. Similar relations can be easily obtained for the holes:

$$\mathcal{G}^h(n,m) = \mathcal{G}^h(m+1,m)\mathcal{G}^h(m+2,m+1)\ldots\mathcal{G}^h(n,n-1) \tag{23}$$

and

$$\mathcal{G}^h(l,l-1) = (\mathcal{B}_l)^{-1}\,\mathcal{G}^h(l,l)\,. \tag{24}$$

The composite properties above allow one to build dynamical Green functions from shorter segments. One can break the original imaginary time interval into segments of arbitrary length, say $(n,n-k)$, which turns the matrix in Eq. (22) into the product of the k matrices $\mathcal{B}_l$ inside the segment. Multiplying the Green functions, which are physical properties, instead of composing the $\mathcal{B}_l$ matrices, provides more accurate and numerically stable results for the dynamical correlations even for large values of the imaginary time. The length of the segments can be chosen for the best balance between numerical stability (requiring short segments) and computational time (less for longer segments). The complexity of this approach scales with the lattice size as $\mathcal{N}_s^3$, since it requires multiplications of matrices of size $\mathcal{N}_s \times \mathcal{N}_s$.

Although we have discussed the formalism in the path-integral AFQMC framework, it can be easily modified for a constrained path approach of open-ended imaginary time projection, which becomes necessary when the sign problem is present. This is sketched in Fig. 1. When back-propagation begins, one records the initial population and their weights, which play the role of $\{|\phi_R\rangle\}$. As the random walk proceeds (imposing the constraint along the path as needed), one keeps track of the sampled auxiliary-fields and their path history, which gives the path $\mathbf{X} = (\mathbf{x}(1),\cdots,\mathbf{x}(M))$ for each descendent walker at time $\beta_{\rm BP} \equiv M\delta\tau$ beyond when BP begins. We must choose $\beta_{\rm BP}$ such that $\beta_{\rm BP} - \tau$ is sufficiently large to project out the ground state from $\langle\phi_T|$. That is, the segment of the path from $l \equiv M - N_\tau$ to M is used to produce $\langle\phi_L|$, using Eq. (11). The remainder, from $\mathbf{x}(1)$ to $\mathbf{x}(N_\tau)$, play the same role as in Eq. (18). Since the entire auxiliary-field configurations (or, equivalently, segments of the propagator matrices) have been recorded along the BP path, we can proceed in the same way as described above to obtain the dynamical Green's functions. As in BP computation of equal-time Green's functions, the weight to be used in the Monte Carlo estimator should be that of the descendent walker at "future time" $\beta_{\rm BP}$.[36]

Once the imaginary-time Green's functions are computed, many correlation functions can be obtained. The charge gap can be computed as we discuss below. Further, the Green's functions are related to the spectral function:

$$A(Q,\omega) = \begin{cases} \sum_n |\langle\Psi_n^{\mathcal{N}_p+1}|\hat{c}^\dagger_{Q,\sigma}|\Psi_0\rangle|^2\delta\left(\omega - \left(E_n^{\mathcal{N}_p+1} - E_0^{\mathcal{N}_p}\right)\right), & \omega > \mu \\ \sum_n |\langle\Psi_n^{\mathcal{N}_p-1}|\hat{c}_{Q,\sigma}|\Psi_0\rangle|^2\delta\left(\omega + \left(E_n^{\mathcal{N}_p-1} - E_0^{\mathcal{N}_p}\right)\right), & \omega < \mu \end{cases} \tag{25}$$

Here $\Psi_n^{\mathcal{N}_p\pm1}$ are the eigenstates of the hamiltonian operator with $\mathcal{N}_p \pm 1$ particles corresponding to the energies $E_n^{\mathcal{N}_p\pm1}$, while μ is the chemical potential. The spectral function is proportional to the imaginary part of the time-ordered Green function. It can be experimentally measured from photoemission and inverse photoemission spectroscopy. The spectral function provides insight into the nature of the single particle spectral weight for a correlated system, and is a central object in many-body theory. From the imaginary-time correlation functions, a Fredholm integral equation has to be solved to determine the spectral function; in practice:

$$\int_\mu^{+\infty} e^{-\tau\omega}A(Q,\omega)d\omega = \frac{\langle\Psi_0|\,\hat{c}_Q\,e^{-\tau(\hat{H}-E_0)}\hat{c}^\dagger_Q\,|\Psi_0\rangle}{\langle\Psi_0\,|\,\Psi_0\rangle} \tag{26}$$

and:

$$\int_{-\infty}^\mu e^{-\tau\omega}A(Q,\omega)d\omega = \frac{\langle\Psi_0|\,\hat{c}^\dagger_Q\,e^{\tau(\hat{H}-E_0)}\hat{c}_Q\,|\Psi_0\rangle}{\langle\Psi_0\,|\,\Psi_0\rangle}\,. \tag{27}$$

The charge gap Δ is typically inferred from the behavior of the zero distance *real-space* Green function for

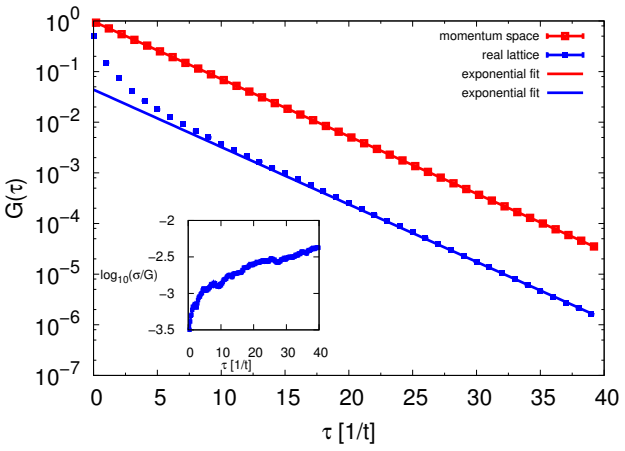

FIG. 2. (color online) Dynamical Green functions in real- and momentum-space, and the dependence of statistical errors on imaginary-time. $G(R,\tau)$ was computed at $R=0$, and $G(Q,\tau)$ at a Q close to the Fermi surface. The system was a 6×6 lattice at half-filling with $U/t=0.5$. In the main figure, statistical errors are much smaller than symbol size. The straight lines are exponential fits to the large imaginary time region (note semi-log scale). The inset shows the dependence of the relative error bar on the imaginary time.

large imaginary time. In general,

$$\Delta = \frac{1}{2}\left(\varepsilon_p + \varepsilon_h\right) \tag{28}$$

with:

$$\varepsilon_{p,h} = -\lim_{\tau\to+\infty} \frac{\log\left(G^{p,h}(R=0,\tau)\right)}{\tau} = E(\mathcal{N}_p\pm 1) - E(\mathcal{N}_p)\,, \tag{29}$$

where $E(\mathcal{N}_p)$ is the ground state energy for N particles, while $E(\mathcal{N}_p\pm 1)$ correspond to the lowest energy eigenstates of the $\mathcal{N}_p\pm 1$ systems having non-zero overlap with the state obtained by adding/removing a particle in any momentum state to the $\mathcal{N}_p$-particle ground state. At half filling, particle-hole symmetry[39] allows us to simplify the above definition:

$$\Delta = -\lim_{\tau\to+\infty} \frac{\log\left(G^{p}(R=0,\tau)\right)}{\tau} - \mu \tag{30}$$

Since the hamiltonian defined in Eq. (1) is particle-hole symmetric, the chemical potential μ is zero at half filling.

We could also compute the gap in *momentum space*:

$$\Delta = \min_{Q}\left(-\lim_{\tau t\to+\infty} \frac{\log\left(\tilde{G}^{p}(Q,\tau)\right)}{\tau}\right)\,. \tag{31}$$

Eq. (31) provides an intuitive physical meaning of the charge gap: Δ is related to the minimum energy among the unoccupied states, which can be probed via inverse photoemission spectroscopy (see, for example, Ref. 40 and references therein), using a collimated beam of electrons directed at the sample. (At half filling, particle-hole symmetry makes this energy coincide with the minimum energy needed to extracting a photoelectron in a direct spectroscopy experiment when the sample is illuminated via electromagnetic radiation.)

Computing the dynamical Green function in momentum space is more convenient than in real space, at least for smaller values of U/t. In this regime $G^p(R=0,\tau)$ contains a linear combination of exponentials while $\tilde{G}^p(Q,\tau)$ has a simpler structure which can be handled more easily via analytic continuation methodologies. It is straightforward to see this in the limiting case of $U=0$, when $\tilde{G}^p(Q,\tau)$ is a single exponential:

$$\tilde{G}^p_0(Q,\tau) = \overline{n}_0(Q)\, e^{-\tau\varepsilon(Q)}\,, \tag{32}$$

where $\overline{n}_0(Q) = 1 - n_0(Q)$, with $n_0(Q)$ being the Fermi distribution. In contrast,

$$G^p_0(R=0,\tau) = \frac{1}{\mathcal{N}_s}\sum_{Q} \overline{n}_0(Q)\, e^{-\tau\varepsilon(Q)}\,, \tag{33}$$

in which the minimum gap ($\varepsilon(Q_F)=0$ in this case, Q_F belonging to the Fermi surface) provides the charge gap at sufficiently large τ but many other exponentials can persist for significant τ values, especially as the system size grows.

In fact we could construct a linear combination to target in order to optimize convergence and statistical accuracy in the computation of the gap:

$$\tilde{G}^p_B(\tau) \propto \sum_{Q\in B} \tilde{G}^p(Q,\tau)\,. \tag{34}$$

One simple definition for the momentum domain in the summation could be $B=\{Q : |\overline{n}(Q) - \overline{n}_0(Q)| > \text{const}\}$, where $\overline{n}(Q) = 1 - n(Q)$ is defined with respect to the momentum distribution of the interacting system, $n(Q)$. The value of const can be tuned.

Even more generally, one could use any single particle orbital $|\mu\rangle$ to create a quasi particle excitation. The real and momentum space shown above are simply two special cases. In the formalism presented above, suitable linear combinations of the dynamical Green functions would be required. This possibility can be particularly useful in the new approach we propose in Sec. IV, where any single-particle orbital (for example a natural orbital obtained from the many-body calculation), can be propagated along with the ground-state random walker with little additional cost.

In Fig. 2 we show an example of calculation of imaginary-time Green functions at half filling with $U/t=0.5$, in both real space and momentum space. It is evident that the two reach the same slope in logarithmic scale at large imaginary time but that $\tilde{G}^p(Q,\tau)$ has a much simpler structure, allowing us to accurately calculate the slope without the need of reaching very large imaginary times. This is important since the relative statistical uncertainty increases exponentially, as shown in the inset.

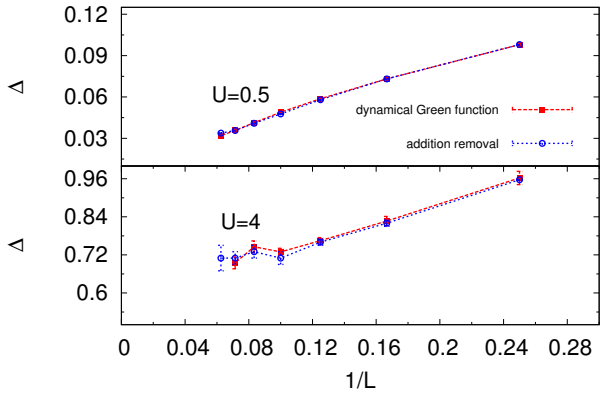

FIG. 3. (color online) Charge gap measured from dynamical Green function (filled squares) and from addition/removal (open circles), as a function of the inverse linear size of the system, $1/L$. The two panels are for two different interaction strengths: $U = 0.5$ (upper) and $U = 4$ (lower).

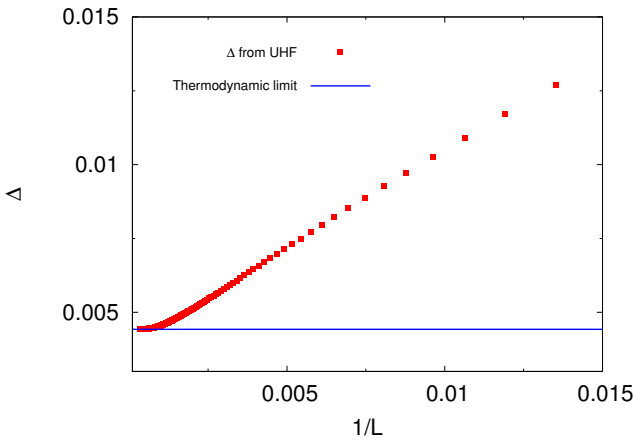

FIG. 4. (color online) Charge gap measured from UHF calculations at $U = 0.5$, as a function of $1/L$. The straight line indicates the UHF gap value at the thermodynamic limit, 0.0044272.

The charge gap can also be estimated with an addition/removal technique, calculating directly ε_p and ε_h in Eq. (28). This approach has the advantage that it does not require the evaluation of dynamical correlation functions. It also has several disadvantages. With three separate calculations (or two, if at half-filling) of $\mathcal{N}_p$ and $\mathcal{N}_p \pm 1$ particles, it involves the difference between extensive quantities, which can give rise to large statistical uncertainties for large systems. Second, while not present in Hubbard-like models, the addition/removal of an electron in a supercell in real solids tends to create a significant additional finite-size effects which requires larger supercells or better correction schemes in the many-body calculation. Moreover, in the Hubbard model at half-filling the systems with $\mathcal{N}_p \pm 1$ particles both have a sign problem, while the (half-filled) $\mathcal{N}_p$ system does not[39].

We have performed addition/removal calculations of the gap to help check the robustness of the imaginary-time Green's function approach. These calculations were performed with the constrained path Monte Carlo (CPMC) method[2,25]. We used trial wave functions obtained from the generalized Hartree-Fock (GHF), which were found to improve the results near half-filling[35,41]. For the $(\mathcal{N}_p - 1)$ calculation, we use the same GHF trial wave function as for half-filling, simply omitting the extra orbital in the minority-spin sector, while the next virtual GHF orbital is used in the $(\mathcal{N}_p + 1)$ case. This was found, by comparison with exact diagonalization results, to give exact results on the gap to within statistical errors.

In Fig. 3 the gaps computed from imaginary-time Green's function and from addition/removal are compared for a variety of systems ranging from 4×4 to 16×16 periodic supercells. Excellent agreement is seen between the two approaches. It is also evident that the gap converges rather slowly with supercell size. Especially at smaller values of U, very large lattices are needed and a fit in $1/L$ is difficult and can be unreliable. We discuss how to obtain more robust estimates at the thermodynamic limit in the next section.

III. GAPS AT THE THERMODYNAMIC LIMIT

A. Approaches to reduce the finite-size effects

To access bulk properties it is crucial to be able to extrapolate the results to the thermodynamic limit. We perform simulations up to lattices containing 24×24 sites, i.e. 576 electrons, more than twice the largest lattice for which dynamical calculations had been performed before. Nevertheless, as shown in Fig. 3, it is still challenging to determine the gap reliably, especially for small values when it is necessary to resolve the existence of a gap. In order to shed light into the behavior for $1/L \to 0$, we performed unrestricted Hartree Fock (UHF) calculations systematically as a function of lattice size. The gaps are obtained by the orbital energies in a Koopman's theorem type of approach for each supercell size. The results are shown in Fig. 4. Note that most of the L values in the data are beyond reach of many-body calculations in supercells with present day computing power. The quantitative (or even qualitative) accuracy of UHF aside, the results illustrate the strong finite-size effects that must be overcome in order to reach the thermodynamic limit accurately.

Our first step to reduce finite-size effects is to use twisted boundary conditions with quasi-random sequences of twist parameters[35]. Formally, the introduction of a twist parameter $\theta = (\theta_x, \theta_y)$, $0 \le \theta_{x,y} < 1$ means that the algebra of creation and destruction operators satisfy the new boundary conditions:

$$\hat{c}^\dagger_{i+L\hat{x}} = e^{i2\pi\theta_x}\,\hat{c}^\dagger_i, \quad \hat{c}^\dagger_{i+L\hat{y}} = e^{i2\pi\theta_y}\,\hat{c}^\dagger_i \qquad (35)$$

for all sites i; $\hat{x}$ and $\hat{y}$ denote the unit vectors in x and y directions. This implies that the wave vectors are $Q_{x,y} =$

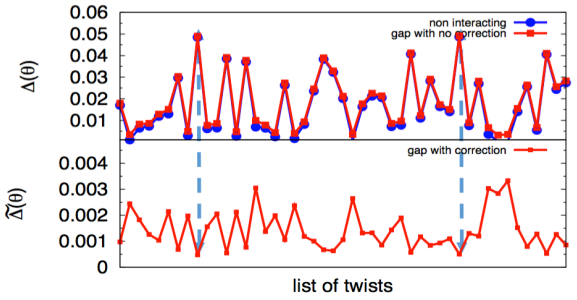

FIG. 5. (color online) Finite-size effects in computing the gap, the use of twist boundary conditions, and special twist values. The top panel shows the non-interacting gap, and the exact many-body gap as a function of the twist parameters. The bottom panel shows the corrected gaps, and identifies the minimum. The system is a 14×14 lattice at $U/t = 0.5$.

$\frac{2\pi}{L}(n_{x,y} + \theta_{x,y})$ or, equivalently, that we can replace the original dispersion relation $\varepsilon(Q)$ with $\varepsilon(Q + \frac{2\pi}{L}\theta)$.

It is known[30] that performing averages of physical quantities, like the ground state energy, with respect to the twist parameter strongly reduces finite-size effects. The discretization of the Fermi "sphere" due to the finite size is smeared out by the presence of the twist parameters. A straightforward application of twist averaging in our calculations yields the results shown in the inset of Fig. 6 for $U/t = 0.5$. The error bars are estimated as a combination of the uncertainty from the analytic continuation for a given twist and the one coming from the twist averaging (obtained with a jackknife estimator). From the plot it is evident that the role of the boundary conditions is important.

We can further improve convergence to the thermodynamic limit by removing the one-body finite-size effect[42,43]. We can correct the values of the computed gap for a given θ by the *finite-size* non-interacting gap, to eliminate or reduce the effects arising purely from the shift of the Fermi sphere and the shell structure. The upper panel of Fig. 5 illustrates this effect, where a strong correlation is evident between the true many-body gap $\Delta(\theta)$ and the non-interacting gap $\Delta^0(\theta)$. The simple correction $\tilde{\Delta}(\theta) = \Delta(\theta) + \left(\Delta^0 - \Delta^0(\theta)\right)$, where $\Delta^0 = 0$ is the non-interacting gap at the thermodynamic limit, gives one order of magnitude reduction in the fluctuations of the gap values. This is expected at small U. We find that, although the dependence on the twist parameter is weaker at, say, $U = 4$, the correlation is also present at larger U. The gap result as a function of system size after the one-body finite-size correction is shown in Fig. 6. We see that the twist-averaged result (averaging $\tilde{\Delta}(\theta)$ over the twist θ, in this case nearly 50 quasi random twist parameters) has much smaller error bars, because of the reduction in the fluctuations between twist parameters mentioned above, and displays better convergence and a quadratic scaling in $1/L$.

We propose a third step for accelerating convergence, involving a different way to use the twisted boundary conditions than the more standard procedure above. After one-body finite-size correction, we seek the minimum gap among all the twist angles

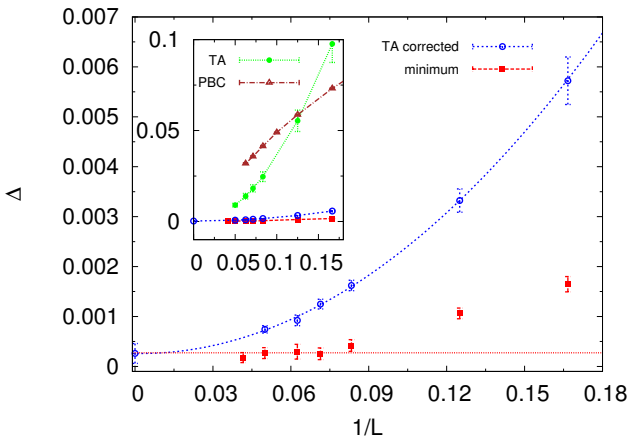

FIG. 6. (color online) Reduction of the finite-size effects and convergence to the thermodynamic limit in computing the charge gap. The charge gap at $U/t = 0.5$ measured from dynamical Green function are shown as a function of $1/L$, from a twist-averaging (TA) procedure together with one-body correction (empty circles) and taking the minimum among the corrected gaps (filled squares). The dotted line is a quadratic fit to the twist-averaged data. The straight line is the estimation of the thermodynamic limit, obtained using the minimum gap estimator performing a linear fit. The inset shows the same data, together with the results from TA prior to the one-body correction are also shown (filled circles) together with those from (PBC) (filled triangles), which contain large finite-size effects.

$$\Delta_{\min} = \min_{\theta} \left(\tilde{\Delta}(\theta) \right) . \tag{36}$$

This allows one to better sample for the minimum in Eq. (31). We stress that the difference between Eq. (36), averaging over $\tilde{\Delta}(\theta)$, and even $\Delta(\theta)$ itself vanishes in the thermodynamic limit. However, taking the minimum among the post-correction twist results enable access to estimations of the values of Eq. (31) for a much larger set of points, which improves the estimation of the minimum. As we see in Fig. 6, this procedure leads to a further improvement over the TA results, with the computed gap becoming essentially flat for $L \gtrsim 12$. Most of our results in the next section are obtained with this procedure of finding the minimum corrected gap. The statistical uncertainties on the minimum corrected gap are estimated simply as the QMC errors; we have checked that this estimation is reliable by performing, in some situations, several independent calculations and computing the variance of $\Delta_{\min}$.

We have examined the location of $\Delta_{\min}$. In the bottom panel of Fig. 5 we have marked the twist angle which yielded the minimum. We find that the corrected gap $\tilde{\Delta}(\theta)$ reaches its minimum when the non-interacting gap is maximum, that is around $\theta_{\min} = (0, 1/2)$ or symmetry-related points. This observation holds for all the cases we have studied, including a variety of lattice sizes L at

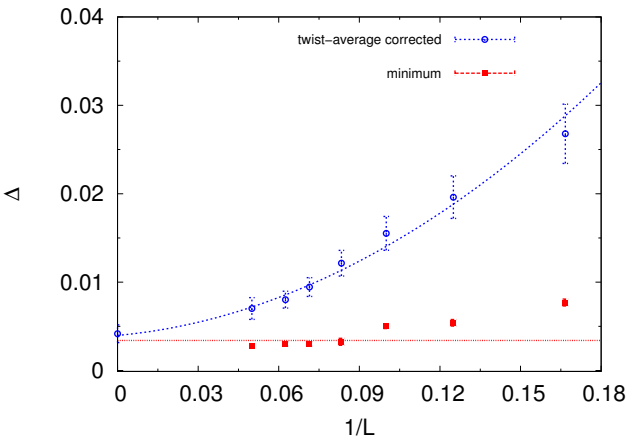

FIG. 7. (color online) Charge gap at $U/t = 1$ vs. the inverse (linear) system size. The gas are measured from dynamical Green function with twist-averaging and one-body correction (empty circles) and with the minimum $\Delta_{\rm min}$ (filled squares). The dotted line is a quadratic fit to the twist-averaged data. The straight line is the estimation of the thermodynamic limit, obtained using the minimum gap estimator.

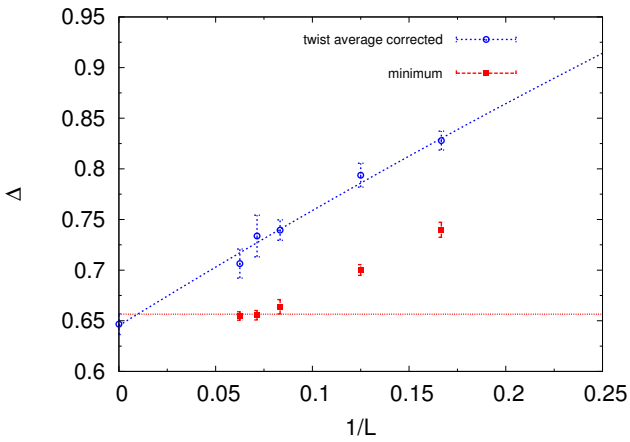

FIG. 8. (color online) Charge gap at $U/t = 4$. Symbols and setup are the same as in Fig. 7.

multiple values of U (0.5, 1, and 4). We rationalize the observation as follows: when a particle is added at half-filling, the system accommodates it by creating a spin wave. The value $\theta_{\rm min} = (0, 1/2)$ allows the maximum wavelength for this excitation, thus allowing the minimum energy. In the next section, we apply this special $\theta_{\rm min}$ to obtain the gap value in many other U values between 0.5 and 4. Of course the particular value of $\theta_{\rm min}$ will depend on the system, but any insight towards identifying its value or narrowing its range will help reduce the computational cost.

B. Results on gaps and the spectral function for the Hubbard model at half-filling

In this section, we present our results of the charge gap in the repulsive Hubbard model at half-filling, systematically as a function of the interaction, as well as the spectral function at $U = 4t$. These calculations are similar to prior efforts that exist to study such quantities, using both the Lanczos method for small lattices[44,45] and QMC for larger lattices[16,17,39]. Our calculations reach larger system sizes and apply the approaches discussed above to systematically reach the thermodynamic limit.

In Fig. 6 we show the final results obtained for $U = 0.5t$. Lattice sizes up to 24×24 were studied using multiple quasi-random twist angles. We find a charge gap of $\Delta = 0.00027(4)$ at the thermodynamic limit. This very small value is clearly impossible to determine using conventional calculations with periodic boundary conditions (PBC) or even twist-averaged boundary conditions (TABC). That the gap value is small but non-zero is significant, confirming that the ground state of the Hubbard model is insulating at small finite U.

In Fig. 7 we show the results of the same calculation for $U/t = 1$. Qualitatively the behavior is the same as for $U = 0.5$. The statistical uncertainties are larger, since $U = 0.5$ is so small that the dynamical Green functions are very similar to the ones of the non-interacting system, which makes the finite-size correction in Eq. (36) especially effective in reducing the statistical uncertainty. Our estimation of the charge gap at $U/t = 1$ is $\Delta = 0.0034(4)$.

We present results for $U/t = 4$ in Fig. 8. In this case, the twist averaged results displays a nearly linear dependence on $1/L$, consistent with results from a previous QMC study[16]. As in the other cases, our estimator from Eq. (36) becomes flat also in this case. Our estimate of the charge gap at $U/t = 4$ is $\Delta = 0.656(2)$.

Next, we map out a detailed Δ vs. U curve by studying a variety of interaction strengths. Having established the $\theta_{\rm min}$ value from the systematic searches at the U values studied above, we now use the special twist value $\theta_{\rm min}$ for each additional system, computing the gap at a sufficiently large L. We have verified in a few systems by calculations at multiple L's that convergence to the thermodynamic limit has been reached. The results are shown in Fig. 9. We find that, at small U, the gap behaves as $\Delta(U) = \alpha \exp\left(-\beta\sqrt{\frac{t}{U}}\right)$, as predicted by UHF[39], with renormalized parameters α and β. We find $\alpha = 0.23(4)$ and $\beta = 4.3(2)$, in contrast with the UHF predictions $\alpha = 32$ and $\beta = 2\pi$. (The actual UHF results are seen to, not surprisingly, severely over-estimate the gap.) On the other hand, at large U/t, the gap appears to follow the same behavior predicted in *one-dimension* from the Bethe ansatz[46]:

$$\Delta_{1D}(U) = \frac{U}{2} - 2 + 4\int_0^{+\infty} d\omega \frac{J_1(\omega)}{\omega(1+\exp(\omega U/2))}\,, \quad (37)$$

where $J_1(\omega)$ is a Bessel function.

Finally, in Fig. 10 we show a calculation of the full spectral function $A(Q, \omega)$ defined in Eq. (25). The horizontal axis shows Q along a path in the Brillouin zone, indicated

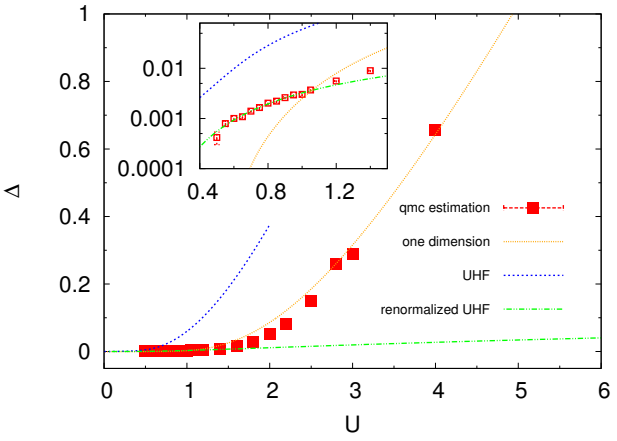

FIG. 9. (color online) Gap at half-filling as a function of the interaction strength. Symbols are obtained from AFQMC calculations. Statistical error bars are shown but are smaller than symbol size. The (green) dashed line corresponds to a fit of the QMC data with a mean-field form allowing renormalized parameters. The (blue) dotted line is the actual mean-field result from unrestricted Hartree-Fock. The (orange) line at large U is the Bethe ansatz prediction for one-dimension. The inset shows a zoom of the main graph at small U.

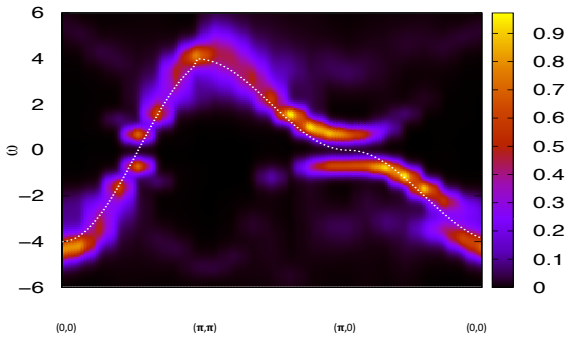

FIG. 10. (color online) Color plot of the spectral function $A(Q,\omega)$ as a function of momentum Q (horizontal axis) along the principal directions in the Brillouin zone and frequency ω (vertical axis). The spectral function has been obtained by performing analytic continuation of the calculated imaginary time Green functions in momentum space. The system was a 16×16 lattice at $U/t = 4$. The dotted line is the non-interacting dispersion relation.

by the end points of the straight-line segments. The spectral function was obtained from analytic continuation of the imaginary-time Green functions, as discussed in Eqs. (26) and (27). The analytic continuation has been performed using the Genetic Inversion via Falsification of Theories (GIFT) method[5]. As mentioned, the spectral function can be measured experimentally via photoemission experiments, and provides a map of the single particle states of the system. From the plot, where the non-interacting spectral function $A^0(Q,\omega) = \delta(\omega - \varepsilon(Q))$ is also shown, the effect of the interactions is evident, with the opening of a gap at the Fermi surface, as well as the broadening and renormalization of the dispersion relation.

IV. NEW METHOD

In this section we propose a new method which will enable faster computations of the Green's functions in a larger number of situations than the method of Sec. II B. In particular, the new method allows us to calculate single matrix elements of the Green's function with a number of operations scaling linearly with lattice sites (or basis size). In systems such as dilute Fermi gas and *ab initio* calculation of realistic systems[2,26], the lattice or basis size is significantly larger than the number of particles, $\mathcal{N}_s \gg \mathcal{N}_p$, so that it is advantageous to be able to calculate the Green functions (and certain correlation functions) with computational cost of $\mathcal{O}(\mathcal{N}_s\mathcal{N}_p^2)$ versus $\mathcal{O}(\mathcal{N}_s^3)$. Even if the calculation of the full Green's function matrix would still require the latter, generally we are interested in in a subset of them, not all the elements. Moreover, as we will show below, the method we are proposing allows to extend the calculation in a straightforward way to two-body dynamical correlations without affecting the complexity.

A. Particle excitations

We consider the estimator in Eq. (18) in a more general sense:

$$g_{\nu,\mu}(\mathbf{X},\tau) = \frac{\langle\phi_L|\,\hat{c}_\nu\,\hat{B}_{N_\tau}\ldots\hat{B}_1\;\hat{c}_\mu^\dagger|\phi_R\rangle}{\langle\phi_L\,|\,\hat{B}_{N_\tau}\ldots\hat{B}_1\,|\,\phi_R\rangle}\,, \qquad (38)$$

where $|\nu\rangle$ and $|\mu\rangle$ are single-particle orbitals, which can be either position eigenstates $|i\rangle$, $|j\rangle$, momentum eigenstates $|Q\rangle$ or even more general states such as natural orbitals.

Let us start from the $\mathcal{N}_p$-particles Slater determinant:

$$|\phi_R\rangle = \hat{c}_{u_1}^\dagger\ldots\hat{c}_{u_{\mathcal{N}_p}}^\dagger\,|0\rangle\,, \qquad (39)$$

where $\hat{c}_u^\dagger = \sum_i\langle i|u\rangle\,\hat{c}_i^\dagger$ creates a particle in the orbital $|u\rangle$. It is convenient to assume that the orbitals $|u_1\rangle,\ldots,|u_{\mathcal{N}_p}\rangle$ form an orthonormal set, which in practice is realized by, for example, a modified Gram-Schmidt (GS) procedure. The creation operator $\hat{c}_\mu^\dagger$ adds to $|\phi_R\rangle$ one particle in the orbital $|\mu\rangle$, giving rise to a new $(\mathcal{N}_p+1)$-particle Slater determinant:

$$|\phi_R^{\mathcal{N}_p+1}\rangle = \hat{c}_\mu^\dagger\,|\phi_R\rangle\,. \qquad (40)$$

Written in orthonormal form:

$$|\phi_R^{\mathcal{N}_p+1}\rangle = \hat{c}^\dagger_{\tilde{\mu}}\hat{c}^\dagger_{u_1}\dots\hat{c}^\dagger_{u_{\mathcal{N}_p}}|0\rangle\,\mathcal{D}_{\mathcal{N}_p+1}\,, \tag{41}$$

where $|\tilde{\mu}\rangle$ is the orbital $|\mu\rangle$ after projecting out the linear dependence on $\{|u\rangle\}$:

$$|\tilde{\mu}\rangle = \frac{\mu - \sum_{\alpha=1}^{\mathcal{N}_p}\langle u_\alpha\,|\mu\,\rangle\,|u_\alpha\rangle}{||\mu - \sum_{\alpha=1}^{\mathcal{N}_p}\langle u_\alpha\,|\mu\,\rangle\,|u_\alpha\rangle||}, \tag{42}$$

with $\mathcal{D}_{\mathcal{N}_p+1} = \langle\tilde{\mu}\,|\mu\rangle$. Now, if a propagator $\hat{B}$ is applied, we have:

$$\hat{B}\,|\,\phi_R\rangle = \hat{c}^\dagger_{\hat{B}u_1}\dots\hat{c}^\dagger_{\hat{B}u_{\mathcal{N}_p}}|0\rangle\,, \tag{43}$$

and

$$\hat{B}|\phi_R^{\mathcal{N}_p+1}\rangle = \hat{c}^\dagger_{\hat{B}\tilde{\mu}}\hat{c}^\dagger_{\hat{B}u_1}\dots\hat{c}^\dagger_{\hat{B}u_{\mathcal{N}_p}}|0\rangle\;\mathcal{D}_{\mathcal{N}_p+1}\,. \tag{44}$$

That is, each orbital is propagated by the one-particle propagator $\hat{B}$, so that both the $\mathcal{N}_p$- and the $(\mathcal{N}_p+1)$-particle Slater determinants remain in form as Slater determinants. In orthonormal form:

$$\hat{B}\,|\,\phi_R\rangle = |\,\phi'_R\,\rangle\,\mathcal{D} \tag{45}$$

with

$$|\,\phi'_R\,\rangle = \hat{c}^\dagger_{u'_1}\dots\hat{c}^\dagger_{u'_{\mathcal{N}_p}}|0\rangle\,, \tag{46}$$

where the orbitals $|u'_1\rangle,\dots,|u'_{\mathcal{N}_p}\rangle$ form an orthonormal set and $\mathcal{D}$ is the factor arising from the GS decomposition, and

$$\hat{B}|\phi_R^{\mathcal{N}_p+1}\rangle = |\phi_R^{\mathcal{N}_p+1\,\prime}\rangle\;\mathcal{D}\;\mathcal{D}'_{\mathcal{N}_p+1}\,\mathcal{D}_{\mathcal{N}_p+1} \tag{47}$$

with:

$$|\phi_R^{\mathcal{N}_p+1\,\prime}\rangle = \hat{c}^\dagger_{\tilde{\mu}'}|\phi'_R\rangle = \hat{c}^\dagger_{\tilde{\mu}'}\hat{c}^\dagger_{u'_1}\dots\hat{c}^\dagger_{u'_N}|0\rangle \tag{48}$$

where, as before, $|\tilde{\mu}'\rangle$ is the orbital $|\hat{B}\tilde{\mu}\rangle$ after projecting out the linear dependence on $\{|u'\rangle\}$, and $\mathcal{D}'_{\mathcal{N}_p+1} = \langle\tilde{\mu}'\,|\hat{B}\tilde{\mu}\rangle$.

This procedure can be iterated for the product of $\hat{B}$ in Eq. (38), propagating the single-particle orbitals and accumulating the weights $\mathcal{D}'$. As in regular AFQMC for static observables, the GS reorthonormalization need not be applied at every iteration, only with a frequency sufficient to ensure numerical stability[25]. The evaluation of the Green's function element requires the calculation of:

$$g_{\nu\mu}(\mathbf{X},\tau) = \mathcal{D}'_{\mathcal{N}_p+1}\mathcal{D}_{\mathcal{N}_p+1}\,\frac{\langle\phi_L|\,\hat{c}_\nu\,\phi_R^{\mathcal{N}_p+1\,\prime}\rangle}{\langle\phi_L\,|\phi'_R\rangle}\,. \tag{49}$$

Applying $\hat{c}_\nu$ to the left, we can evaluate the numerator as the overlap of two $(\mathcal{N}_p+1)$-particle Slater determinants. Equivalently:

$$g_{\nu\mu}(\mathbf{X},\tau) = \mathcal{D}'_{\mathcal{N}_p+1}\mathcal{D}_{\mathcal{N}_p+1}\,\frac{\langle\phi_L|\,\hat{c}_\nu\,\hat{c}^\dagger_{\tilde{\mu}'}\,|\,\phi'_R\rangle}{\langle\phi_L\,|\phi'_R\rangle}\,. \tag{50}$$

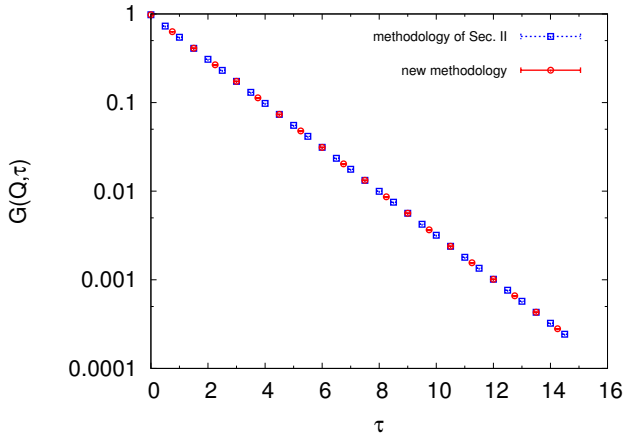

FIG. 11. (color online) Particle Green function $\tilde{G}(Q,\tau)$ for a large lattice in the repulsive Hubbard model: comparison between the new methodology and that described in Sec. II B. A 12×12 lattice with 72 spin-↑ and 72 spin-↓ particles is studied at $U/t=1$.

In explicit matrix representation, if we denote:

$$\Phi'_R = \begin{pmatrix} \langle 1|u'_1\rangle & \dots & \langle 1|u'_{\mathcal{N}_p}\rangle \\ \langle 2|u'_1\rangle & \dots & \langle 2|u'_{\mathcal{N}_p}\rangle \\ \langle 3|u'_1\rangle & \dots & \langle 3|u'_{\mathcal{N}_p}\rangle \\ \dots & \dots & \dots \\ \dots & \dots & \dots \\ \langle \mathcal{N}_s|u'_1\rangle & \dots & \langle \mathcal{N}_s|u'_{\mathcal{N}_p}\rangle \end{pmatrix} \tag{51}$$

and

$$\Phi_L = \begin{pmatrix} \langle 1|v_1\rangle & \dots & \langle 1|v_{\mathcal{N}_p}\rangle \\ \langle 2|v_1\rangle & \dots & \langle 2|v_{\mathcal{N}_p}\rangle \\ \langle 3|v_1\rangle & \dots & \langle 3|v_{\mathcal{N}_p}\rangle \\ \dots & \dots & \dots \\ \dots & \dots & \dots \\ \langle \mathcal{N}_s|v_1\rangle & \dots & \langle \mathcal{N}_s|v_{\mathcal{N}_p}\rangle \end{pmatrix} \tag{52}$$

for $\langle\phi_L| = \langle 0|\,\hat{c}_{v_{\mathcal{N}_p}}\dots\hat{c}_{v_{\mathcal{N}_p}}$, simple algebraic manipulations allow us to obtain the ratio on the right Eq. (50), the matrix element, as

$$\left(\langle\nu\,|\tilde{\mu}'\rangle - \sum_{\alpha,\beta=1}^{\mathcal{N}_p}\langle\nu\,|u'_\alpha\rangle\,\langle u'_\beta\,|\tilde{\mu}'\rangle\left((\mathbf{\Phi_L})^\dagger\;\mathbf{\Phi'_R}\right)^{-1}_{\alpha,\beta}\right)\,, \tag{53}$$

which can be evaluated with $\mathcal{O}(\mathcal{N}_s\,\mathcal{N}_p^2)$ operations for a given pair of $|\tilde{\mu}'\rangle$ and $|\nu\rangle$.

In Fig. 11 we show a comparison between the particle Green's function computed using the method discussed in Sec. II B and the one computed with the present method. The perfect agreement shows the robustness of both approaches. As mentioned, the savings from the present method occur when a small number of Green's function elements are targeted. When the whole Green's function is needed, the approach becomes more computationally expensive. Also, the advantage relies on $\mathcal{N}_p \ll \mathcal{N}_s$, so that at half-filling as in Fig. 11, for example, there is no

advantage over the previous method. On the other hand, in the dilute limit the reduction in computational cost (and potentially in memory requirement as well, since the propagated determinants are of size $\mathcal{O}(\mathcal{N}_s\mathcal{N}_p)$ vs. $\mathcal{O}(\mathcal{N}_s^2)$ for $\mathcal{G}$) can be dramatic, such as in systems of cold atoms[27] and especially with spin-orbit coupling present[47] which further increases the basis size.

B. Hole excitations

Suppose now we wish to compute the estimator:

$$h_{\nu,\mu}(\mathbf{X},\tau) = \frac{\langle\phi_L|\,\hat{c}_\nu^\dagger\,\hat{B}_{N_\tau}\ldots\hat{B}_1\;\hat{c}_\mu|\phi_R\rangle}{\langle\phi_L\,|\,\hat{B}_{N_\tau}\ldots\hat{B}_1\,|\,\phi_R\rangle}\,. \tag{54}$$

We again consider $\hat{c}_\mu$ acting on $|\phi_R\rangle$:

$$|\phi_R^{\mathcal{N}_p-1}\rangle = \hat{c}_\mu\,|\,\phi_R\rangle = \hat{c}_\mu\,\hat{c}_{u_1}^\dagger\ldots\hat{c}_{u_{\mathcal{N}_p}}^\dagger\,|0\rangle\,, \tag{55}$$

which is no longer a single Slater determinant, but a linear combination of $\mathcal{N}_p$ Slater determinants. However, because these determinants all have the same structure, each containing $(\mathcal{N}_p-1)$ orbitals taken from $|\phi_R\rangle$, their propagation by a propagator $\hat{B}$ can be handled together in a convenient way.

We re-write Eq. (55) as

$$|\phi_R^{\mathcal{N}_p-1}\rangle = \hat{c}_{\tilde{\mu}}\hat{c}_{u_1}^\dagger\ldots\hat{c}_{u_{\mathcal{N}_p}}^\dagger\,|0\rangle\,, \tag{56}$$

where $|\tilde{\mu}\rangle$ is the projection of $|\mu\rangle$ onto the linear space spanned by $|u_1\rangle,\ldots,|u_{\mathcal{N}_p}\rangle$:

$$|\tilde{\mu}\rangle = \sum_{\alpha=1}^{\mathcal{N}_p}\langle\mu\,|\,u_\alpha\rangle\,|\,u_\alpha\rangle\,. \tag{57}$$

The propagation of $|\,\phi_R\rangle$ in the denominator in Eq. (54) is identical to that in the previous section, Sec. IV A. For the numerator, it follows from simple algebraic manipulations[38]:

$$\hat{B}|\phi_R^{\mathcal{N}_p-1}\rangle = \hat{c}_{\left(\hat{B}^{-1}\right)^\dagger|\tilde{\mu}\rangle}\hat{c}_{\hat{B}u_1}^\dagger\ldots\hat{c}_{\hat{B}u_{\mathcal{N}_p}}^\dagger\,|0\rangle \tag{58}$$

The orbital $|\tilde{\mu}\rangle$ evolves under the action of $\left(\hat{B}^{-1}\right)^\dagger$, since it corresponds to a destruction operator.

After reorthonormalization of in Eqs. (45) and (46), we can re-write

$$\hat{B}|\phi_R^{\mathcal{N}_p-1}\rangle = |\phi_R^{\mathcal{N}_p-1\,\prime}\rangle\;\mathcal{D} \tag{59}$$

with:

$$|\phi_R^{\mathcal{N}_p-1\,\prime}\rangle\; = \hat{c}_{\tilde{\mu}'}|\phi_R'\rangle = \hat{c}_{\tilde{\mu}'}\hat{c}_{u_1'}^\dagger\ldots\hat{c}_{u_{\mathcal{N}_p}'}^\dagger\,|0\rangle\,, \tag{60}$$

where $|\tilde{\mu}'\rangle$ is the projection of the orbital $(\hat{B}^{-1})^\dagger\,|\tilde{\mu}\rangle$ onto the linear space of $\{|u'\rangle\}$, as in Eq. (57). The evaluation of the hole Green's function in Eq. (54) now becomes:

$$h_{\nu\mu}(\mathbf{X},\tau) = \frac{\langle\phi_L|\,\hat{c}_\nu^\dagger\,\phi_R^{\mathcal{N}_p+1\,\prime}\rangle}{\langle\phi_L\,|\phi_R'\rangle} = \frac{\langle\phi_L|\,\hat{c}_\nu^\dagger\,\hat{c}_{\tilde{\mu}'}\,|\,\phi_R'\rangle}{\langle\phi_L\,|\phi_R'\rangle}\,. \tag{61}$$

Simple algebraic manipulations in the matrix representation of Eqs. (51) and (52) allow us to express the matrix element on the right as:

$$\sum_{\alpha,\beta=1}^{\mathcal{N}_p}\langle\tilde{\mu}'\,|u_\alpha'\rangle\,\langle u_\beta'\,|\nu\rangle\,\left((\mathbf{\Phi_L})^\dagger\;\mathbf{\Phi_R'}\right)^{-1}_{\alpha,\beta}\,. \tag{62}$$

C. Two-body correlation functions

Suppose we wish to compute a density-density or a spin-spin correlation function. In both cases, we have to compute:

$$n(\mathbf{X},\tau) = \frac{\langle\phi_L|\,\hat{n}_{j,\sigma'}\,\hat{B}_{N_\tau}\ldots\hat{B}_1\;\hat{n}_{i,\sigma}|\phi_R\rangle}{\langle\phi_L\,|\,\hat{B}_{N_\tau}\ldots\hat{B}_1\,|\,\phi_R\rangle} \tag{63}$$

where $\hat{n}_{i,\sigma} = \hat{c}_{i,\sigma}^\dagger\hat{c}_{i,\sigma}$ is the fermion density operator. In this case, we will write explicitly the spin index.

We will exploit the following exact property

$$\hat{n}_{i,\sigma} = \frac{e^{\hat{n}_{i,\sigma}}-1}{e-1} \tag{64}$$

which can be easily proved by expanding the exponential operator and noting $\hat{n}_{i,\sigma}^2 = \hat{n}_{i,\sigma}$. Thus the numerator in Eq. (63) can be viewed as propagating two Slater determinants.

If $|\phi_R\rangle = \hat{c}_{|u_1,\uparrow\rangle}^\dagger\ldots\hat{c}_{|u_{N_\uparrow},\uparrow\rangle}^\dagger\hat{c}_{|v_1,\downarrow\rangle}^\dagger\ldots\hat{c}_{|v_{N_\downarrow},\downarrow\rangle}^\dagger|0\rangle$, the identity in Eq. (64) provides the following (for example in the spin-up case):

$$\hat{n}_{i,\uparrow}|\phi_R\rangle = \frac{|\phi_R'(i)\rangle - |\phi_R\rangle}{e-1} \tag{65}$$

where:

$$|\phi_R'(i)\rangle = \hat{c}_{|e^{\hat{n}_{i,\uparrow}}u_1,\uparrow\rangle}^\dagger\ldots\hat{c}_{|e^{\hat{n}_{i,\uparrow}}u_{N_\uparrow},\uparrow\rangle}^\dagger\hat{c}_{|v_1,\downarrow\rangle}^\dagger\ldots\hat{c}_{|v_{N_\downarrow},\downarrow\rangle}^\dagger|0\rangle\,. \tag{66}$$

The application of the one-body propagator $e^{\hat{n}_{i,\uparrow}}$ on the orbitals can be carried out straightforwardly. Now, the estimator Eq. (63) can be broken into two pieces:

$$n(\mathbf{X},\tau) = \frac{1}{e-1}\left(n_1(\mathbf{X},\tau) - n_2(\mathbf{X},\tau)\right)\,, \tag{67}$$

which can be conveniently expressed as:

$$n_1(\mathbf{X},\tau) = \frac{\langle\phi_L|\,\hat{n}_{j,\sigma'}\hat{B}\;|\phi_R'(i)\rangle}{\langle\phi_L\,|\hat{B}\;|\,\phi_R'(i)\rangle}\;\frac{\langle\phi_L|\,\hat{B}\;|\phi_R'(i)\rangle}{\langle\phi_L\,|\hat{B}\;|\,\phi_R\rangle} \tag{68}$$

and:

$$n_2(\mathbf{X},\tau) = \frac{\langle\phi_L|\,\hat{n}_{j,\sigma'}\hat{B}\;|\phi_R\rangle}{\langle\phi_L\,|\hat{B}\;|\,\phi_R\rangle} \tag{69}$$

Both $n_1(\mathbf{X},\tau)$ and $n_2(\mathbf{X},\tau)$ can be readily calculated. As usual, GS decomposition can be applied periodically in the propagation of $|\phi_R\rangle$ and $|\phi_R'\rangle$ to ensure numerically stability.

V. CONCLUSIONS

We study the calculation of dynamical correlation functions in imaginary time using auxiliary-field quantum Monte Carlo. The use of twisted-boundary conditions is systematically explored. One-body finite-size corrections help improve the convergence to the thermodynamic limit. We study the role of special twists which correspond to the minimum corrected gap, and show that this dramatically reduces finite-size effects. In the repulsive Hubbard model at half-filling, the charge gaps and spectral functions are computed for different interaction strengths. Much higher accuracy was reached than previously possible, especially for small gap values. We propose a new approach to compute the imaginary-time Green's functions by explicitly varying the number of particles in the QMC random walk. This method has several advantages, including a much more favorable computational cost in "dilute" systems where the size of the basis is significantly larger than the number of fermions (from cubic to linear in lattice/basis size).

VI. ACKNOWLEDGMENTS

We thank Huy Nguyen for his contributions at early stages of this work. This work was supported by NSF (Grant No. DMR-1409510). E.V. and S. Z. were also supported by the Simons Foundation. Computing was carried out at the Extreme Science and Engineering Discovery Environment (XSEDE), which is supported by National Science Foundation grant number ACI-1053575, and the computational facilities at William and Mary.

[1] W. M. C. Foulkes, L. Mitas, R. J. Needs, and G. Rajagopal, Rev. Mod. Phys. **73**, 33 (2001).
[2] S. Zhang, *Auxiliary-Field Quantum Monte Carlo for Correlated Electron Systems*, Vol. 3 of *Emergent Phenomena in Correlated Matter: Modeling and Simulation*, Ed. E. Pavarini, E. Koch, and U. Schollwöck (Verlag des Forschungszentrum Jülich, 2013).
[3] F. F. Assaad, *Quantum Monte Carlo Methods on Lattices: The Determinantal Method* , Lecture Notes of the Winter School on Quantum Simulations of Complex Many-Body Systems: From Theory to Algorithms, Vol. 10 (John von Neumann Institute for Computing, Jülich, 2002).
[4] G. H. Booth, A. J. W. Thom, and A. Alavi, The Journal of Chemical Physics **131**, 054106 (2009), http://dx.doi.org/10.1063/1.3193710.
[5] E. Vitali, M. Rossi, L. Reatto, and D. E. Galli, Phys. Rev. B **82**, 174510 (2010).
[6] M. Rossi, E. Vitali, L. Reatto, and D. E. Galli, Phys. Rev. B **85**, 014525 (2012).
[7] R. Rota, F. Tramonto, D. E. Galli, and S. Giorgini, Phys. Rev. B **88**, 214505 (2013).
[8] M. Nava, D. E. Galli, M. W. Cole, and L. Reatto, J Low Temp Phys **171**, 699 (2012).
[9] S. Saccani, S. Moroni, E. Vitali, and M. Boninsegni, Mol. Phys. **109**, 2807 (2011).
[10] S. Saccani, S. Moroni, and M. Boninsegni, Phys. Rev. Lett. **108**, 175301 (2012).
[11] S. Molinelli, D. E. Galli, L. Reatto, and M. Motta, Journal of Low Temperature Physics , 1 (2016).
[12] F. Arrigoni, E. Vitali, D. E. Galli, and L. Reatto, Low Temp. Phys. **39**, 793 (2013).
[13] G. Bertaina, M. Motta, M. Rossi, E. Vitali, and D. E. Galli, Phys. Rev. Lett. **116**, 135302 (2016).
[14] J. E. Hirsch, Phys. Rev. B **31**, 4403 (1985).
[15] M. Feldbacher and F. F. Assaad, Phys. Rev. B **63**, 073105 (2001).
[16] F. F. Assaad and M. Imada, Phys. Rev. Lett. **76**, 3176 (1996).
[17] D. Rost, E. V. Gorelik, F. Assaad, and N. Blümer, Phys. Rev. B **86**, 155109 (2012).
[18] G. H. Booth and G. K.-L. Chan, The Journal of Chemical Physics **137**, 191102 (2012), http://dx.doi.org/10.1063/1.4766327.
[19] M. Nava, D. E. Galli, S. Moroni, and E. Vitali, Phys. Rev. B **87**, 144506 (2013).
[20] M. Motta, D. E. Galli, S. Moroni, and E. Vitali, The Journal of Chemical Physics **140**, 024107 (2014).
[21] M. Motta, D. E. Galli, S. Moroni, and E. Vitali, The Journal of Chemical Physics **143**, 164108 (2015), http://dx.doi.org/10.1063/1.4934666.
[22] J. W. Moskowitz, K. E. Schmidt, M. A. Lee, and M. H. Kalos, The Journal of Chemical Physics **77** (1982).
[23] P. J. Reynolds, D. M. Ceperley, B. J. Alder, and W. A. Lester, The Journal of Chemical Physics **77** (1982).
[24] W. M. C. Foulkes, L. Mitas, R. J. Needs, and G. Rajagopal, Rev. Mod. Phys. **73**, 33 (2001).
[25] S. Zhang, J. Carlson, and J. E. Gubernatis, Phys. Rev. Lett. **74**, 3652 (1995).
[26] S. Zhang and H. Krakauer, Phys. Rev. Lett. **90**, 136401 (2003).
[27] H. Shi, S. Chiesa, and S. Zhang, Phys. Rev. A **92**, 033603 (2015).
[28] H. Shi and S. Zhang, Phys. Rev. E **93**, 033303 (2016).
[29] J. E. Hirsch, Phys. Rev. B **38**, 12023 (1988).
[30] C. Lin, F. H. Zong, and D. M. Ceperley, Phys. Rev. E **64**, 016702 (2001).
[31] F. Werner and Y. Castin, Phys. Rev. A **86**, 013626 (2012).
[32] J. Hubbard, Proceedings of the Royal Society of London A: Mathematical, Physical and Engineering Sciences **276**, 238 (1963).
[33] M. C. Gutzwiller, Phys. Rev. Lett. **10**, 159 (1963).
[34] H. Shi and S. Zhang, Phys. Rev. B **88**, 125132 (2013).
[35] M. Qin, H. Shi, and S. Zhang, ArXiv e-prints (2016), arXiv:1605.09421 [cond-mat.str-el].
[36] W. Purwanto and S. Zhang, Phys. Rev. E **70**, 056702 (2004).
[37] D. R. Hamann and S. B. Fahy, Phys. Rev. B **41**, 11352 (1990).
[38] B. M. Rubenstein, S. Zhang, and D. R. Reichman, Phys. Rev. A **86**, 053606 (2012).
[39] J. E. Hirsch, Phys. Rev. B **31**, 4403 (1985).

[40] A. Damascelli, Z. Hussain, and Z.-X. Shen, Rev. Mod. Phys. **75**, 473 (2003).
[41] J. P. F. LeBlanc, A. E. Antipov, F. Becca, I. W. Bulik, G. K.-L. Chan, C.-M. Chung, Y. Deng, M. Ferrero, T. M. Henderson, C. A. Jiménez-Hoyos, E. Kozik, X.-W. Liu, A. J. Millis, N. V. Prokof'ev, M. Qin, G. E. Scuseria, H. Shi, B. V. Svistunov, L. F. Tocchio, I. S. Tupitsyn, S. R. White, S. Zhang, B.-X. Zheng, Z. Zhu, and E. Gull (Simons Collaboration on the Many-Electron Problem), Phys. Rev. X **5**, 041041 (2015).
[42] P. R. C. Kent, R. Q. Hood, A. J. Williamson, R. J. Needs, W. M. C. Foulkes, and G. Rajagopal, Phys. Rev. B **59**, 1917 (1999).
[43] H. Kwee, S. Zhang, and H. Krakauer, Phys. Rev. Lett. **100**, 126404 (2008).
[44] E. Dagotto, F. Ortolani, and D. Scalapino, Phys. Rev. B **46**, 3183 (1992).
[45] P. W. Leung, Z. Liu, E. Manousakis, M. A. Novotny, and P. E. Oppenheimer, Phys. Rev. B **46**, 11779 (1992).
[46] E. H. Lieb and F. Y. Wu, Phys. Rev. Lett. **20**, 1445 (1968).
[47] H. Shi, P. Rosenberg, S. Chiesa, and S. Zhang, Phys. Rev. Lett. **117**, 040401 (2016).